Applied Catalysis B: Environmental 330 (2023) 122643

Contents lists available at ScienceDirect

Applied Catalysis B: Environmental

journal homepage: www.elsevier.com/locate/apcatb

Refining electronic properties of Bi_2MoO_6 by In-doping for boosting overall nitrogen fixation via relay catalysis

Taoxia Ma [a,1], Chunming Yang [a,*,1], Li Guo [a], Razium Ali Soomro [b], Danjun Wang [a,*], Bin Xu [a,b,**], Feng Fu [a,*]

[a] Shaanxi Key Laboratory of Chemical Reaction Engineering, College of Chemistry & Chemical Engineering, Yan'an University, Yan'an 716000, PR China

[b] State Key Laboratory of Organic-Inorganic Composites Beijing Key Laboratory of Electrochemical Process and Technology for Materials, Beijing University of Chemical Technology, Beijing 100029, PR China

ARTICLE INFO

Keywords:
In-doped Bi_2MoO_6
Refining electronic properties
Photocatalytic nitrogen fixation
Overall nitrogen fixation
Relay catalysis

ABSTRACT

Modern agriculture and the chemical industries rely heavily on ammonia and nitrate-based products. However, the classic Haber-Bosch and Ostwald processes are extremely energy-consuming and environmentally damaging. Herein, we proposed In-doped Bi_2MoO_6 photocatalyst to achieve "overall nitrogen fixation" via relay catalysis ($N_2 \rightarrow NH_3/NH_4^+ \rightarrow NO_3^-$). Density functional theory (DFT) supported the partial substitution of Bi^{3+} with In^{3+} in Bi_2MoO_6. The density of states further testified that In^{3+} doping has significantly altered the D-band center, achieving a lower energy barrier for N_2 chemisorption/activation and the subsequent hydrogenation reaction at the H_2O/In-doped Bi_2MoO_6 interface. The experiment revealed that using N_2 and H_2O as feedstock, 5% In-Bi_2MoO_6 realized 1.4 folds higher charge-carrier density under illumination with expedited spatial separation/transfer and extended charge-carrier lifespan compared to Bi_2MoO_6. The photocatalyst attained the NH_3 production rate of 53.4 μmol·g^{-1}·h^{-1} at 5% In-Bi_2MoO_6, which was 13-fold higher than Bi_2MoO_6 (4.1 μmol·g^{-1}·h^{-1}) while the NO_3^- production rate reached 54 μmol·g^{-1}·h^{-1}. This work overcame the thermodynamic barrier of N_2 being first reduced to NH_3/NH_4^+, then further oxidized to NO_3^- products, realizing "overall nitrogen fixation", opening a new avenue toward developing clean, energy-saving, and cost-effective ammonia and nitrate production.

1. Introduction

Ammonia is a significant fertilizer for agriculture and a potential energy source for zero-carbon fuels [1–3]. Simultaneously, nitrate is extensively employed in modern agriculture, metallurgy, textiles, energy, and military applications [4–6]. Currently, industrial production of NH_3 is carried out using the Haber Bosch process, which requires high temperatures (673–873 K) and high pressure (15–25 MPa), while nitric acid is synthesized using the Ostwald ammonia oxidation process, which likewise is an energy-consuming reaction with carbon dioxide emissions [7–9]. Photocatalytic nitrogen fixation has emerged as a possible alternative to fossil fuels to convert N_2 and H_2O into NH_3 using direct solar energy. Nevertheless, the photocatalytic efficiency of many catalysts for this process remains poor owing to their inability to exceed the high-energy threshold for N_2 adsorption/activation while simultaneously providing six consecutive electrons to reduce the N_2 molecule. More importantly, previous methods had focused more on synthetic ammonia methods and rarely on the "overall nitrogen fixation" process ($N_2 \rightarrow NH_3/NH_4^+ \rightarrow NO_3^-$) [10]. It is known to all that the "overall nitrogen fixation" process is difficult to drive nitrogen reduction reaction (NRR) and ammonia oxidation reaction (AOR) simultaneously due to the stability of the N≡N triple bond.

To achieve "overall nitrogen fixation", a photocatalyst with a rational energy bandgap is required to drive oxygen evolution reaction (OER) and NRR by coupling of activated N_2 with generated H^+ and electrons (e^-). As a typical Aurivillius-phase Bi-based catalyst [11–13], Bi_2MoO_6 with a tunable band gap has emerged as a promising material to fulfil the OER and NRR half-reactions. The high overpotential of Bi_2MoO_6 for the

* Corresponding authors.
** Corresponding author at: Shaanxi Key Laboratory of Chemical Reaction Engineering, College of Chemistry & Chemical Engineering, Yan'an University, Yan'an 716000, PR China.
E-mail addresses: chunmingyang@yau.edu.cn (C. Yang), wangdj761118@163.com (D. Wang), binxumail@163.com (B. Xu), yadxfufeng@126.com (F. Fu).
[1] These authors contributed equally to this work.

https://doi.org/10.1016/j.apcatb.2023.122643
Received 28 December 2022; Received in revised form 4 March 2023; Accepted 14 March 2023
Available online 15 March 2023
0926-3373/

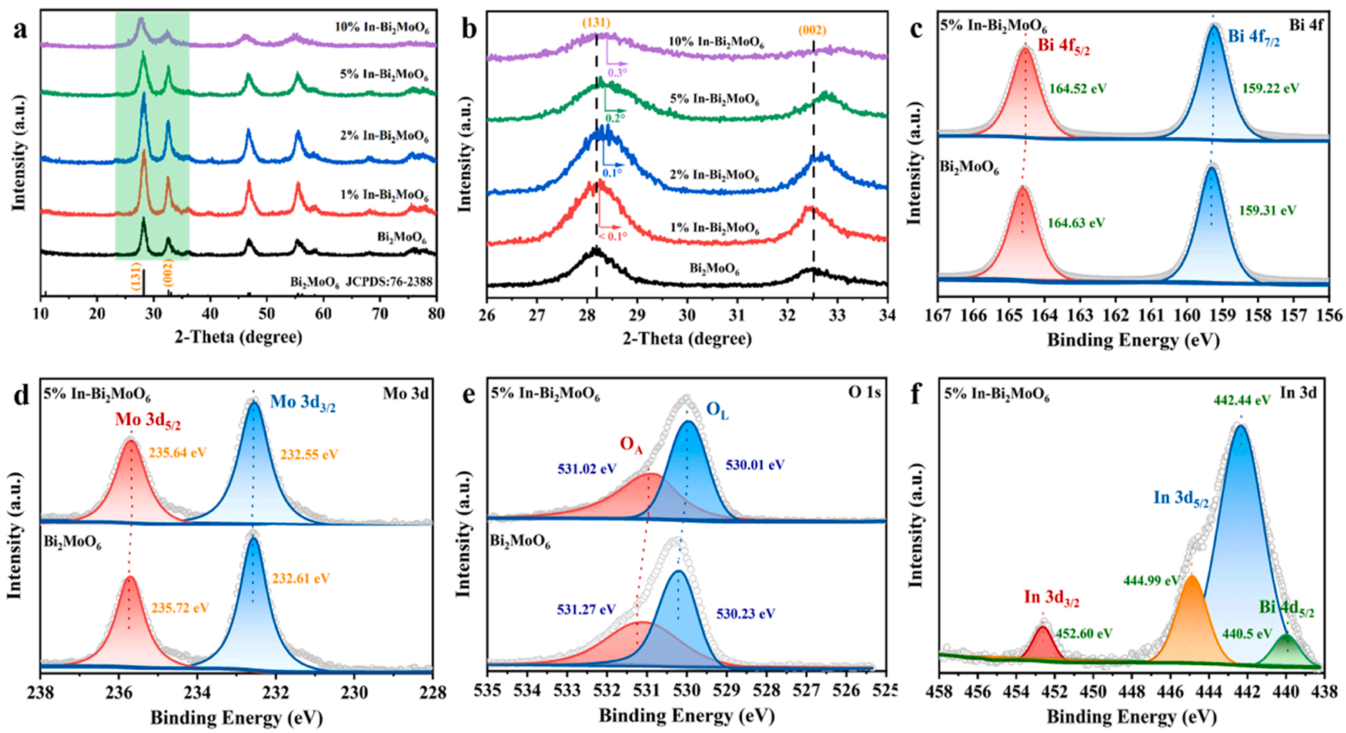

Fig. 1. (a) The XRD patterns of as-prepared samples, (b) The magnified XRD patterns of (131) and (002) crystal planes are in the range of 24–36°. XPS spectra of Bi_2MoO_6 and 5% In-Bi_2MoO_6 sample: (c) Bi 4 f, (d) Mo 3d, (e) O 1 s, (f) In 3d.

hydrogen evolution reaction (HER) (approximately 1.1 V) is particularly advantageous in restricting surface HER reaction, making it more active and selective towards NRR [14,15]. For example, Hao et al. [16] reported a Bi_2MoO_6 with high surface activation capability toward N_2. Despite its ability to achieve NRR, the photocatalyst had poor efficiency owing to its high photogenerated carriers recombination and restricted light response [17].

In order to improve the photocatalytic N_2 fixation efficiency of photocatalysts, it was modified by element doping, defect engineering, construction of heterojunction, and noble metal deposition. Among all, doping photocatalysts with transition metal elements via chemical or physical means have shown promising outcomes in altering their energy band structure. For example, Bo et al. [18] constructed Fe-doped TiO_2 nanofibers to stabilize oxygen vacancies and simultaneously tune their local electronic structure. Similarly, Qiu et al. [19] demonstrated improved N_2 adsorption/activation over Mo-doped $W_{18}O_{49}$ nanowires with rational structure and defect engineering. Accordingly, the precise engineering of elemental doping is crucial for achieving sustained photocatalytic N_2 fixation. Among the variety of metal ions, Indium-ions (In^{3+}) might be an appropriate doping element for Bi_2MoO_6 owing to its relatively smaller ionic radius (0.08 nm) than Bi^{3+} ions (0.103 nm) [20]. The direct doping of In^{3+} in Bi_2MoO_6 could be anticipated to replace Bi^{3+} ions of $[Bi_2O_2]^{2+}$ layers, inducing lattice deformation and changes to its electronic structure [21]. Therefore, the doping of In^{3+} with Bi_2MoO_6 is expected to promote the OER and NRR two half-reactions, achieving N_2 molecule reducted to ammonia and further converted into nitrate (AOR), which will prospectively achieve "overall nitrogen fixation" under mild conditions.

Herein, we present a rationally designed and constructed In-doped Bi_2MoO_6 using a one-step solvothermal route for photocatalytic "overall nitrogen fixation" reaction. The experimental and DFT results demonstrated that In-doping can regulate D-band center of Bi_2MoO_6, boost generation and transportation of photogenerated carriers, and achieve a lower energy barrier for N_2 chemisorption/activation, enabling efficient "overall nitrogen fixation". In-doped Bi_2MoO_6 realized efficient NRR and AOR with NH_3/NH_4^+ and NO_3^- product yields of 53.4 and 54 $\mu mol \cdot g^{-1} \cdot h^{-1}$, respectively. The work offers new insights into the bottleneck issue of artificial nitrogen fixation using a promising photocatalyst with the ultimate goal of attaining efficient "overall nitrogen fixation".

2. Experimental section

2.1. Materials syntheses

In-doped Bi_2MoO_6 was synthesized by the solvothermal method. Typically, $Bi(NO_3)_3 \bullet 5\ H_2O$ (0.97 g, 2 mmol) and $Na_2MoO_4 \bullet 2\ H_2O$ (0.24 g, 1 mmol) were homogenized in 40 mL of ethylene glycol (EG) and 10 mL ethyl alcohol solution under vigorous stirring. The solution was then introduced, 0.0029 g of $InCl_3 \cdot 4\ H_2O$, and stirred for another 30 min before being put into a 100 mL Teflon-lined autoclave made of stainless steel and heated for two hours at 190 °C. After filtering and thoroughly washing with deionized water and absolute ethanol, the products were obtained by drying the material at 60 °C for 12 h. The In-content was changed between 0.0029, 0.0058, 0.0145, and 0.029 g to obtain optimally doped Bi_2MoO_6. The final materials were thus denoted as x% In-Bi_2MoO_6 (where x is the mole ratio of $InCl_3 \cdot 4\ H_2O$ and Bi_2MoO_6) ($x = 1$, 2, 5, and 10). For example, when 0.0029 g of $InCl_3 \cdot 4\ H_2O$ was used, the formed product was 1% In-Bi_2MoO_6. For comparison, pristine Bi_2MoO_6 was synthesized similarly without adding $InCl_3 \cdot 4\ H_2O$.

2.2. Characterization

The phase composition of the prepared samples was examined with powder X-ray diffraction (Shimadzu XRD-7000). X-ray photoelectron spectroscopy (XPS) was carried out using a PHI-5400 (America PE) 250 XI system with Al Kα X-rays as the excitation source. The morphological and structural evaluation was carried out via scanning electron microscopy (SEM) (JEOL (JSM-7610 F)) and transmission electron microscope (TEM) (JEOLF200). The UV-Vis diffuse reflectance spectra (UV-Vis DRS) were measured on a UV-2550 UV-Vis Spectrophotometer with $BaSO_4$ as a reference. Brunauer-Emmett-Teller (BET) surface area was analyzed

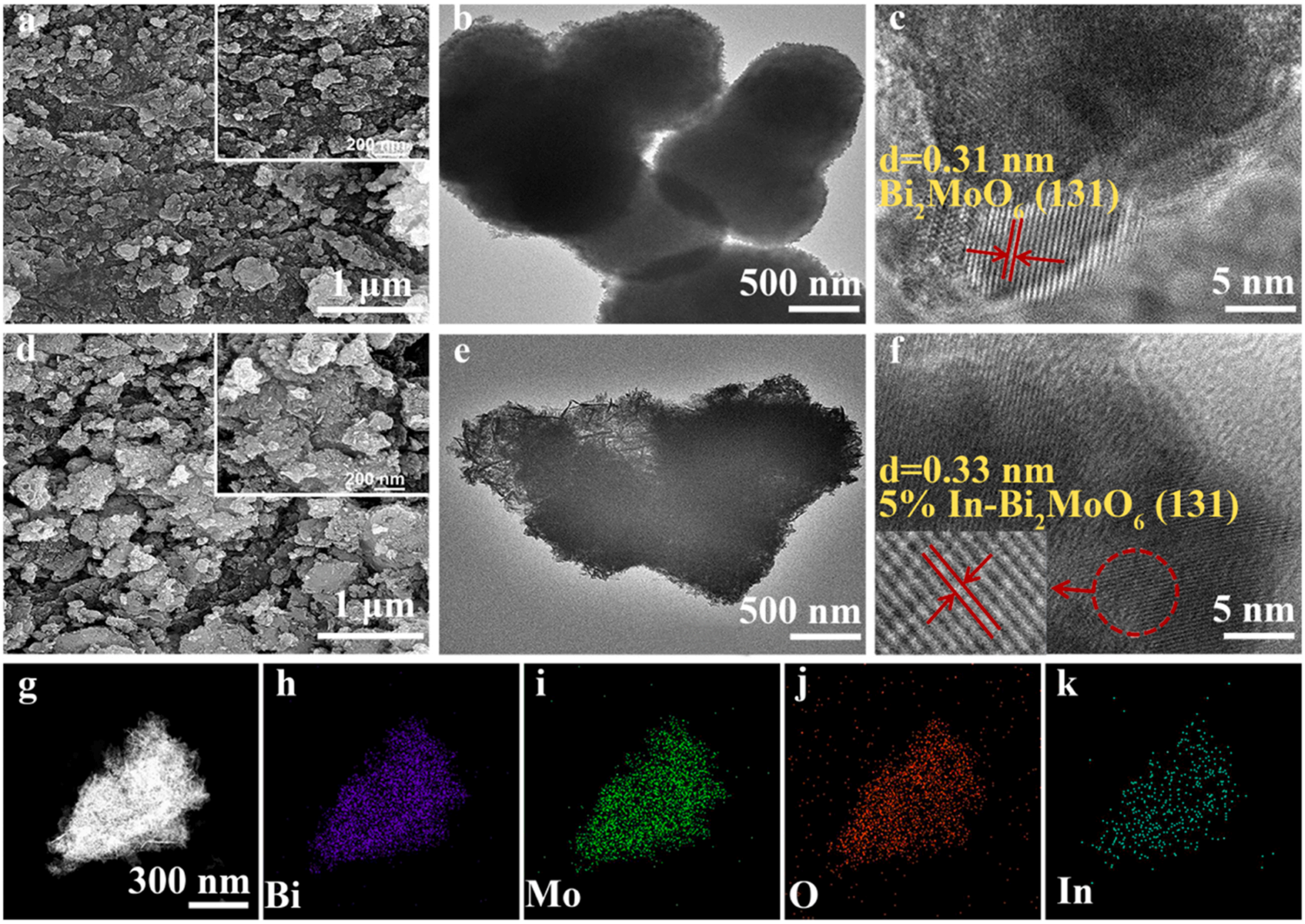

Fig. 2. SEM, TEM, and HRTEM images of (a-c) Bi_2MoO_6, and (d-f) 5% In-Bi_2MoO_6, (g-k) HAADF-TEM image and EDX mapping showing Bi, Mo, O and In as major elements.

using BELSORP MaxII. Nitrogen temperature-programmed desorption (N_2-TPD) was conducted on a Micromeritics AutoChem II 2920 instrument. The photoluminescence (PL) spectroscopy was conducted on an F-4500 spectrophotometer (Hitachi, Japan). Time-resolved photoluminescence (TR-PL) spectra were conducted on an FLS920 fluorescence spectrometer (Edinburgh Analytical Instruments, UK). The in situ DRFTIRS spectra were recorded by in situ FT-IR spectrometer (Bruker Tensor II). The electron spin resonance (ESR) measurements were performed on a JES-FA300 model spectrometer (Japan JEOL, Tokyo, Japan) under visible light irradiation ($\lambda \geq 420$ nm).

2.3. Electrochemical analysis

Photoelectrochemical measurements were performed on a CHI 660E electrochemical workstation (CHENHUA, China) with a three-electrode system and 0.5 M Na_2SO_4 as the electrolyte. Fluoride tin oxide (FTO) was used as a conductive glass substrate for the working electrode, with Ag/AgCl and platinum as the reference and counter electrode, respectively. The working electrode was fabricated by spin coating an active materials slurry (5 mg of sample in a mixture of DI water (1 mL) and ethanol (1 mL)) on FTO glass (2×2 cm^2) and dried at 60 °C overnight. A 300 W Xe lamp (PLS-SXE300D) with a wavelength-dependent cutoff filter (420 nm) at an intensity of 200 mW/cm^2 was used as a light source.

2.4. Photocatalytic nitrogen fixation measurement

The nitrogen fixation was achieved by sonicating 100 mg of photocatalyst in 100 mL of deionized water for 5 min, then transferring the solution to a reactor equipped with a water-cooling system. The suspension solution was vigorously agitated for 30 min in the dark and bubbled with high-purity nitrogen to eliminate dissolved oxygen before being irradiated with a 300 W Xe lamp (30.72 $mW \cdot cm^{-2}$) as the simulated sunlight source, and at the room temperature of 25 °C. Every 30 min during the irradiation, an aliquot (5 mL) of the mixture was taken out and filtered through a 0.22 μm MCE membrane before the production was determined. NH_3/NH_4^+, hydrazine (N_2H_4), and nitrate (NO_3^-) concentrations were determined using Nessler's reagent colorimetric technique, Watt and Chrisp, and the national method (GB/T 5750.8–2006.39.1). The isotope labeling studies were conducted in a high-pressure reactor (WGHX-XH50) with a flowing water outer jacket for temperature control and a quartz window for light irradiation. The apparent quantum yield (AQY) was also detected and calculated. More details are supported in the supporting material (S1.1–1.5).

2.5. In-situ infrared experiment

The sample was placed in a reaction cell and purged with high-purity Ar or N_2 for 30 min to remove surface impurities. After the sample has reached adsorption equilibrium, in the N_2 atmosphere, the samples were illuminated with a xenon lamp and recorded every 5 min

2.6. Density-functional theory (DFT) calculation

The DFT calculation was carried out using the Vienna Ab initio Simulation Package (VASP). For the density of state (DOS), the generalized gradient approximation (GGA) with PBE functional was utilized,

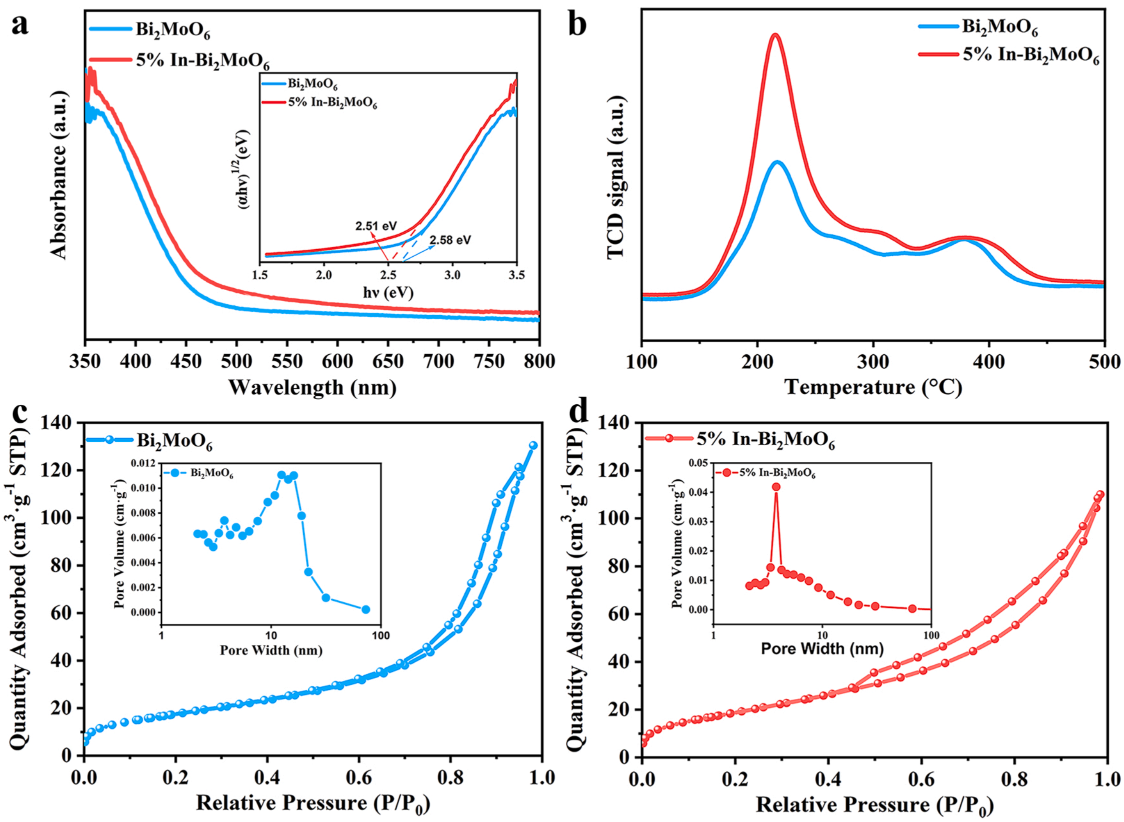

Fig. 3. (a) UV-Vis absorption spectrum and corresponding Tauc plots (inset) of Bi_2MoO_6 and 5% In-Bi_2MoO_6, (b) N_2-TPD curves, (c-d) N_2 sorption isotherms and (inset) pore-size distribution of Bi_2MoO_6 and 5% In-Bi_2MoO_6.

and a plane-wave expansion for the basis set with a cutoff energy of 450 eV was applied. All structural optimizations involved spin-polarization computations. The Gibbs free energy change (ΔG) for each elemental step was calculated using the computational hydrogen electrode model and the proton-coupled electron transfer approach proposed by Nøskov and co-workers. More calculation details are supported in the supporting material (S1.6).

3. Results and discussion

3.1. Morphology and structure of In-doped Bi_2MoO_6 photocatalyst

The crystal structure of pristine Bi_2MoO_6 and In-doped Bi_2MoO_6 was investigated using XRD analysis. Fig. 1a demonstrates that the diffraction peaks for Bi_2MoO_6 were indexed to the orthorhombic Bi_2MoO_6 structure (JCPDS Card No. 76–2388) [22,23], whereas In-doped Bi_2MoO_6 realized a similar pattern with a modest shift for the typical (131) peak that expanded as the In concentration increased. It can be seen in the amplifying XRD patterns (Fig. 1b) that the position of (131) peak shift to the right after In^{3+} doping. This peak shift was attributed to the replacement of Bi^{3+} ions (0.10 nm) with smaller In^{3+} in the main crystal, leading to the change of electrical structure and lattice. As the In^{3+} concentration rises, this shift becomes obvious, demonstrating successful In doping into the crystal of Bi_2MoO_6 [24]. The XPS spectra was employed to investigate the composition and surface chemical state of photocatalysts. The XPS survey spectra shown in Fig. S1 confirm that Bi, Mo, O, and In are the major elements in 5% In-Bi_2MoO_6. However, both Bi_2MoO_6 and 5% In-Bi_2MoO_6 exhibit the similar characteristic peak because the binding energies of In 3d and Bi 4d are very similar. Fig. 1c shows the characteristic binding energy peaks of Bi^{3+} from 5% In-Bi_2MoO_6 compared to its In-free counterpart (Bi_2MoO_6). Bi 4 $f_{7/2}$ and Bi 4 $f_{5/2}$ had fitting Bi^{3+} binding energies of 159.31 and 164.63 eV, respectively, which in the case of 5% In-Bi_2MoO_6 shifted to 159.22 and 164.52 eV, as a result of the interaction between In and Bi_2MoO_6 [25]. The Mo^{6+} was fitted for Mo $3d_{3/2}$ and Mo $3d_{5/2}$ binding energy at 232.55 and 235.64 eV (Fig. 1d), whereas the O 1 s spectra (Fig. 1e) were separated into two primary peaks, 531.02 and 530.01 eV, both of which are attributed to absorbed oxygen, and lattice oxygen, respectively [26, 27]. Furthermore, the binding energy of In exhibits three peaks at 452.60, 444.99, and 442.44 eV that belong to In $3d_{3/2}$, In $3d_{5/2}$. (Fig. 1f), respectively, which indicates the chemical state of In^{3+} [28], while the pristine Bi_2MoO_6 presents no In^{3+} characteristic peaks in the observation region, which confirms the In^{3+} state of indium in In-Bi_2MoO_6. It is worth mentioning that the characteristic peak located at binding energy of around 440.5 eV corresponds to the Bi $4d_{5/2}$ in $Bi_2M_OO_6$ [25], which is very similar to that In $3d_{5/2}$ (Fig. 1f).

The SEM indicated that Bi_2MoO_6 (Figs. 2a) and 5% In-Bi_2MoO_6 (Fig. 2d) had an irregular nanosheet-like structure of the same form and size, suggesting that In-doping had no substantial morphological implications. Fig. 2b, e shown the TEM and HRTEM images of these nanosheets where Bi_2MoO_6 lattice spacing at (131) plane increased from 0.31 nm to 0.33 nm after doping (5% In) (Figs. 2c, 2f). The elemental mapping of 5% In-Bi_2MoO_6 further confirmed the uniform distribution of In^{3+} throughout the photocatalyst (Figs. 2g-2k). The SEM and corresponding EDX spectra of 5% In-Bi_2MoO_6 were also provided in Fig. S2a-b.

The UV–vis DRS was used to evaluate the photocatalyst's optical characteristics and band gap. Fig. 3a shows that the absorption edge of the Bi_2MoO_6 sample red-shifts from 493 nm to 516 nm as In-doping approaches 5%. The Tauc plot (Fig. 3a, inset) shows that the band gap of 5% In-Bi_2MoO_6 reduces from 2.58 to 2.51 eV, indicating that the doped photocatalyst has improved light absorption characteristics than Bi_2MoO_6 [29]. Fig. 3b shows the N_2-TPD curves of Bi_2MoO_6 and 5% In-Bi_2MoO_6. Two major temperature regions which correspond to N_2

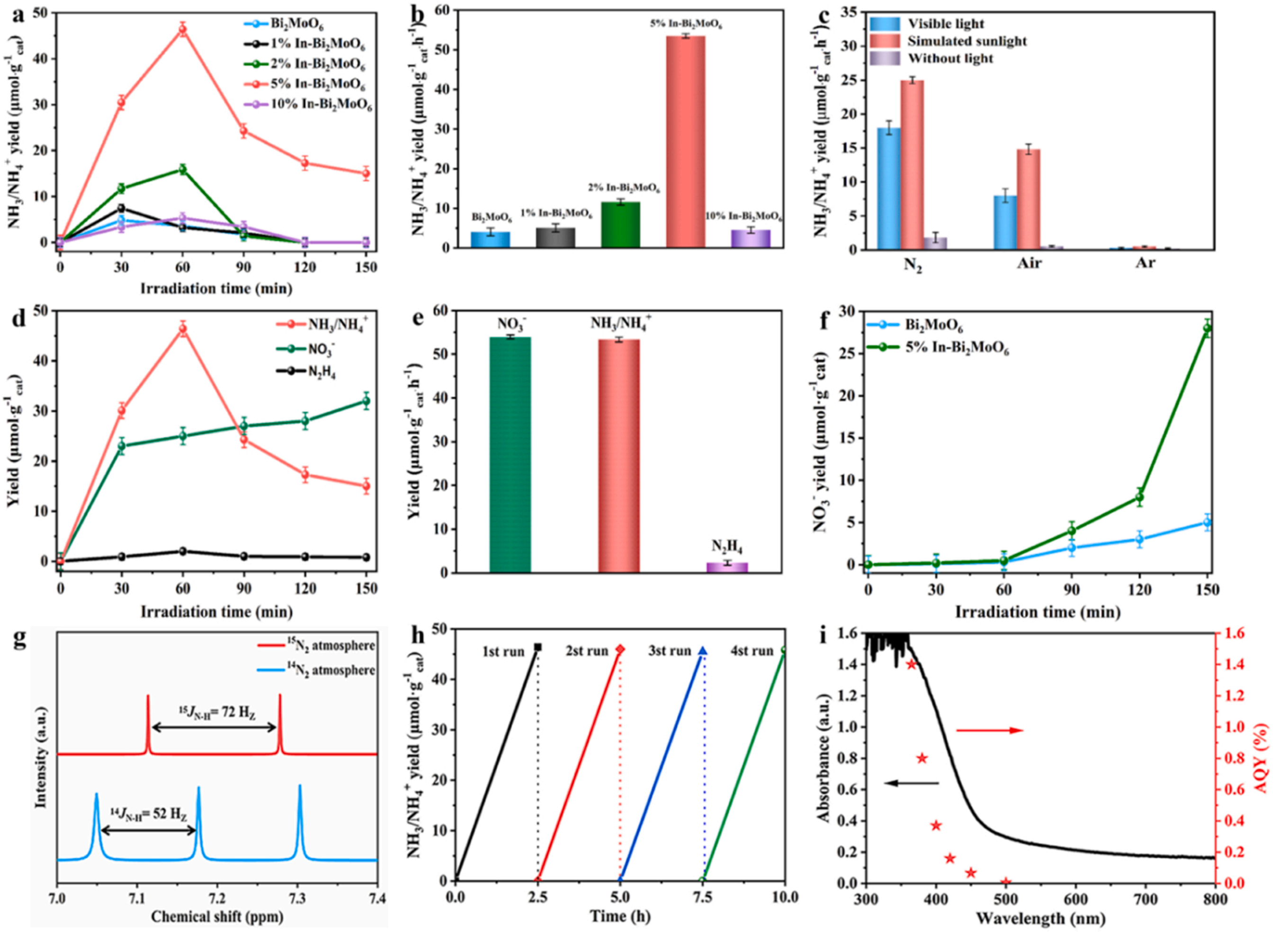

Fig. 4. (a) Photocatalytic N_2 fixation performance, (b) NH_3/NH_4^+ production rate, and (c) NH_3/NH_4^+ yield for Bi_2MoO_6 and its In-doped counterpart with different In content within N_2, Air or Ar atmosphere as the feedstock after 2 h of visible light and simulated sunlight irradiation, (d) The photocatalytic yield of NH_3/NH_4^+, NO_3^- and N_2H_4 using 5% In-Bi_2MoO_6, (e) Different products rate of 5% In-Bi_2MoO_6, and (f) Corresponding yield using Bi_2MoO_6 and 5% In-Bi_2MoO_6 using NH_4Cl as feedstock, (g) ^1H NMR spectra for produced NH_4^+ using N_2 ($^{14}N_2$ or $^{15}N_2$) and water as feedstock, (h) Photocatalytic cycling of 5% In-Bi_2MoO_6 for NH_3/NH_4^+ yield, (i) The variation of abs in relation to AQY of NH_3 evolution over 5% In-Bi_2MoO_6.

physical (200–250 ℃) and chemical adsorption (300–450 ℃) were observed, where the physisorption and chemisorption peaks of 5% In-Bi_2MoO_6 were much higher than those of Bi_2MoO_6, reflecting its improved N_2 adsorption and activation ability [30]. The N_2 sorption isotherms and pore-size distribution (inset) of Bi_2MoO_6 and 5% are shown in Fig. 3c,d. The presence of type-IV isotherms with type-H3 hysteresis loops in Bi_2MoO_6 verified its mesoporous nature [31]. The BET based specific surface area of 5% In-Bi_2MoO_6 was estimated to be 71.09 $m^2 \cdot g^{-1}$, which was 1.1 times larger than Bi_2MoO_6 (64.46 $m^2 \cdot g^{-1}$) with a larger pore volume of 0.20 $cm^3 \cdot g^{-1}$ compared to Bi_2MoO_6 (0.17 $cm^3 \cdot g^{-1}$). The increased surface area and pore volume of 5% In-Bi_2MoO_6 should facilitate N_2 chemisorption activation and surface reaction [32].

3.2. Photocatalytic nitrogen fixation activity of In-doped Bi_2MoO_6

Photocatalytic "overall nitrogen fixation" was performed using 5% In-Bi_2MoO_6 as a photocatalyst under simulated sunlight, using N_2 and H_2O as feedstock (Fig. 4a). The concentrations of NH_3/NH_4^+, hydrazine (N_2H_4), and nitrate (NO_3^-) were determined using Nessler's reagent colorimetric technique (Fig. S3), Watt and Chrisp (Fig. S4), and the national method (GB/T 5750.8–2006.39.1) (Fig. S5), respectively. As shown in Figs. 4b, 5% In-Bi_2MoO_6 had the best NH_3 production rate of 53.4 $\mu mol \cdot g^{-1} \cdot h^{-1}$ comparison with other In^{3+} doping amount, which was 13 times more than Bi_2MoO_6 (4.1 $\mu mol \cdot g^{-1} \cdot h^{-1}$) in N_2 saturated atmosphere. Obviously, the effect of doping amount of In element on the photocatalytic N_2 fixation performance of Bi_2MoO_6 meet the volcanic type law. The excessive In^{3+} doping tends to form the recombination center of electron/hole pairs, resulting in reduced photocatalytic N_2 fixation activity.

Furthermore, using air as a nitrogen supply, ammonia production rates of 35 and 28 $\mu mol \cdot g^{-1} \cdot h^{-1}$ were obtained under simulated sunlight and visible light irradiation, which was much lower than those obtained using an N_2 atmosphere. Table S1 compares the photocatalytic performance of the 5% In-Bi_2MoO_6 with other reported materials. As seen, 5% In-Bi_2MoO_6 offers higher ammonia and nitrate production rates than other competitive materials, signifying the In-doping ability to alter the photocatalytic performance of Bi_2MoO_6 favourably. Fig. 4c shows that ammonia yield is maximum under simulated sunlight and N_2 atmosphere compared to visible light, Ar, and air atmosphere. When there is no light, ammonia is almost undetectable in N_2, air, and Ar atmospheres, highlighting the importance of the illumination in ammonia generation. Interestingly, the NO_3^- production rate (54 $\mu mol \cdot g^{-1} \cdot h^{-1}$) rises progressively as the NH_3/NH_4^+ production rate declines (Fig. 4d), while the N_2H_4 production rate stays under 1% after 1 h of irradiation (Fig. 4e). The NO_3^- production rates of Bi_2MoO_6 with different In doping amounts also exhibited the similar volcanic type law (Fig. S6). It is proved by comparative experiment in Fig. 4 f, NO_3^- is derived from NH_3 oxidation

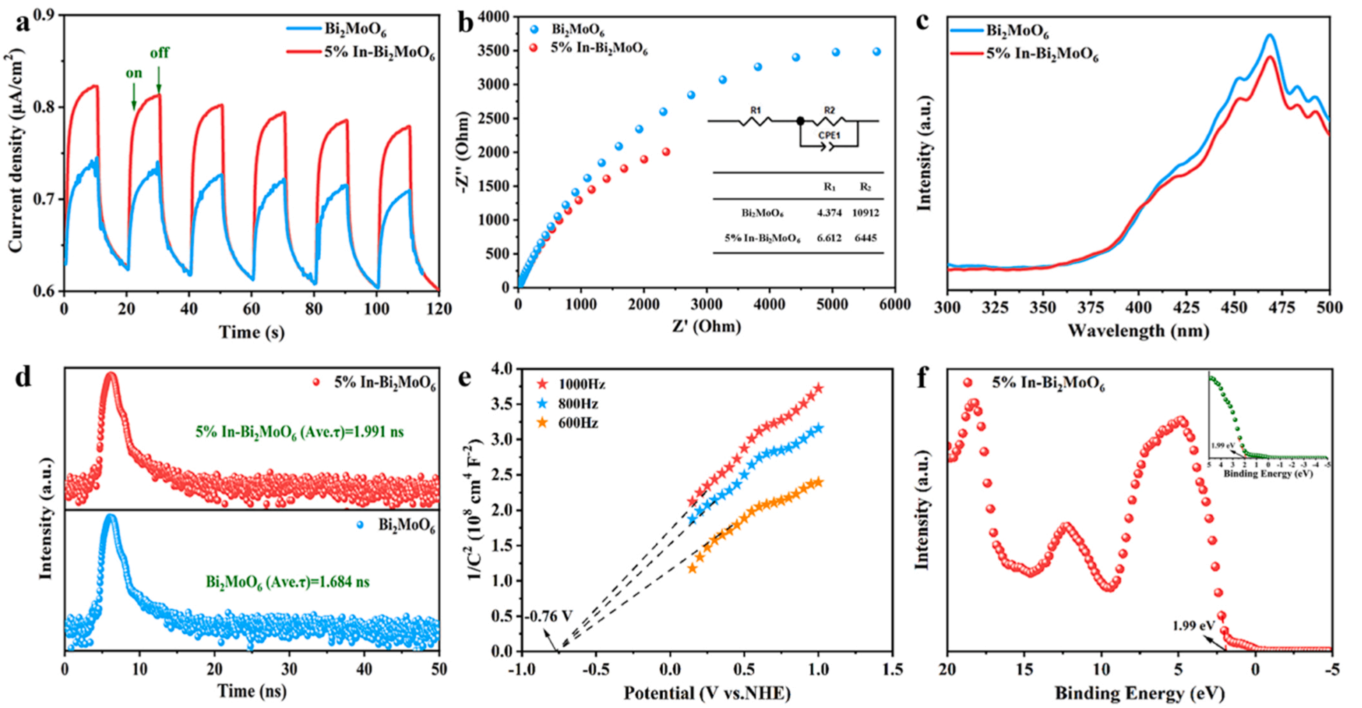

Fig. 5. (a) Transient photocurrent response, (b) EIS Nyquist plots, and (insert table for resistance), (c) PL spectra, and (d) Time-resolved PL decay spectra for 5% In-Bi_2MoO_6 and Bi_2MoO_6, (e) Mott-Schottky plots and (f) VB-XPS spectra depicting the VB and CB position of 5% In-Bi_2MoO_6.

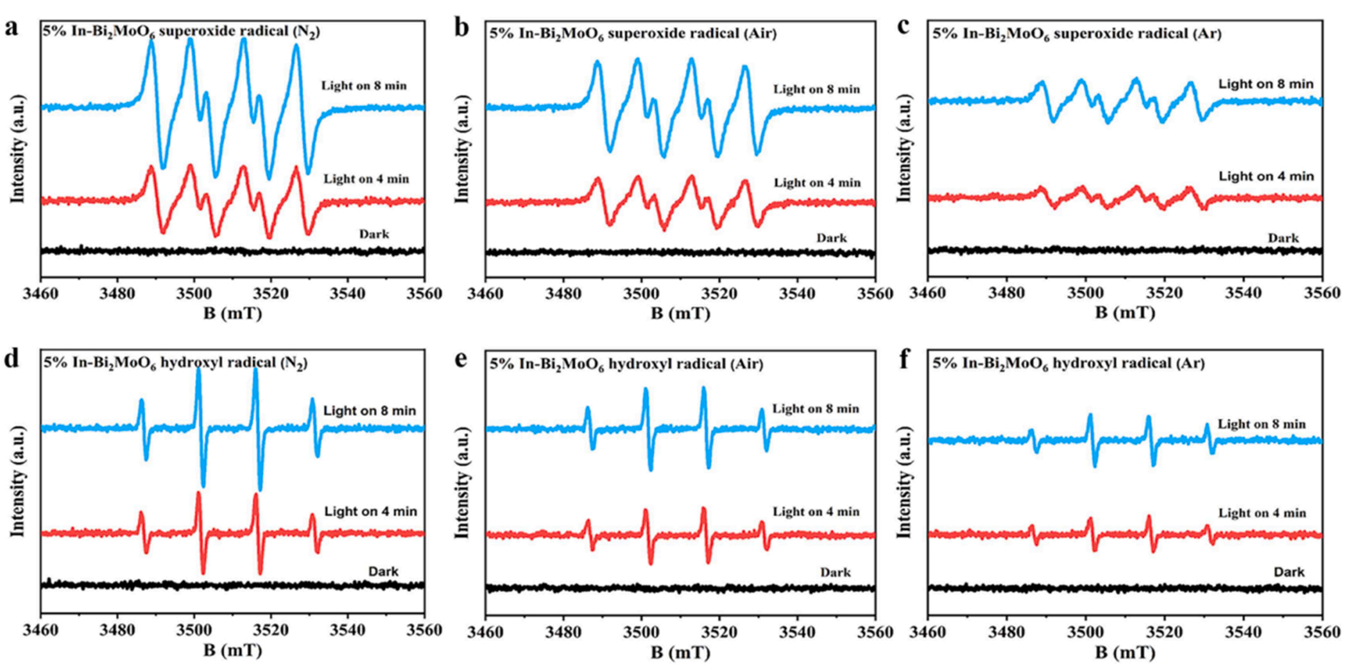

Fig. 6. DMPO spin-trapping ESR spectra of $\bullet O_2^-$ in (a) N_2, (b) Air, and (c) Ar atmospheres and the spectra of •OH radical in (d) N_2, (e) Air, and (f) Ar, atmospheres under visible light irradiation using 5% In-Bi_2MoO_6.

($NH_3/NH_4^+ \rightarrow NO_3^-$) rather than N_2 directly oxidation. The standard molar Gibbs energy of NRR and N_2 directed oxidation/NN_3 oxidation to NO_3^- at 298.15 K was estimated according to Eq. 1, with resultant energies shown as Eqs. 2–4.

$$\Delta_r G^\theta{}_m = \sum_B \nu_B \Delta_f G^\theta{}_m(B) \tag{1}$$

$$N_2 + 6H^+ + 6e^- = 2NH_3 \Delta G = -16.64 KJ \cdot mol^{-1} \tag{2}$$

$$NH_3 + 3H_2O = NO_3{}^- + 9H^+ + 8e^- \Delta G = -101.9 KJ \cdot mol^{-1} \tag{3}$$

$$\frac{1}{2}N_2 + 3H_2O = NO_3{}^- + 6H^+ + 5e^- \Delta G = 602.5 KJ \cdot mol^{-1} \tag{4}$$

Where $\Delta_f G_m^\theta(B)$ is the standard molar Gibbs energy of the individual components of the reaction with thermodynamic data, and ν_B is the measuring coefficient where reactant and product had positive and

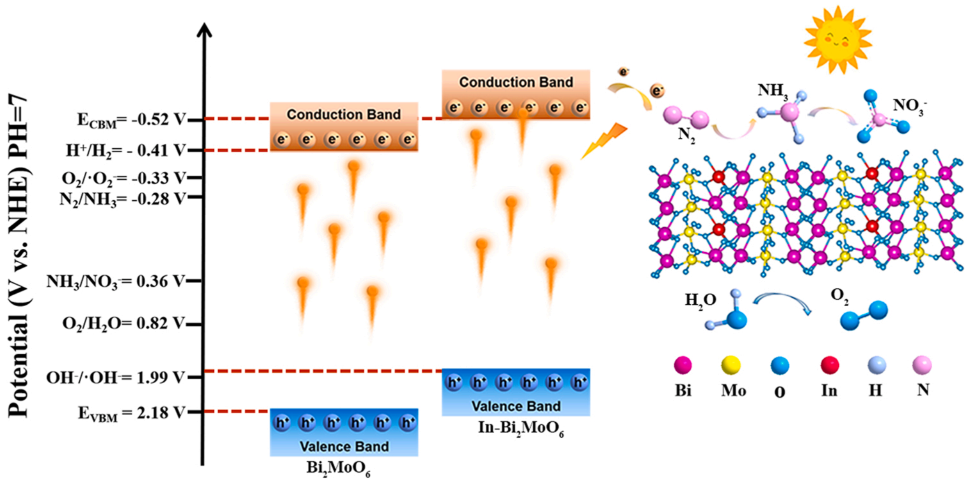

Fig. 7. Schematic illustration of the band structure for working 5% In-Bi_2MoO_6 photocatalyst under illumination. The band gap energy (E_g) of 5% In-Bi_2MoO_6 was estimated from the Tauc plots using the Kubelka-Munk equation, and the CBM values (V vs. NHE) were determined from the Mott-Schottky plots. The VBM value was thus estimated using equation $E_g = E_{VBM}$ - E_{CBM}.

negative values, respectively.

The NH_3 oxidation reaction (Eq. 3) is substantially more negative (-101.9 KJ·mol^{-1}) than that of N_2 with H_2O to form NH_3 (Eq. 2), implying that NH_3 oxidation is more likely to occur, whereas the reaction between N_2 with H_2O to form NO_3^- has a more positive $\Delta_r G_m^\theta$ (Eq. 4), suggesting that direct N_2 oxidation to NO_3^- is impossible. Thus, it is thermodynamically more feasible to reduce N_2 to NH_3 and then further oxidize NH_3 to NO_3^- demonstrating the potential of relay catalysis for overall nitrogen fixation ($N_2 \rightarrow NH_3/NH_4^+ \rightarrow NO_3^-$).

An isotopic labeling experiment using $^{15}N_2$ as the nitrogen source was carried out to ensure that the N element in ammonia originates from N_2 reduction. When the $^{15}N_2$ was utilized as the nitrogen source for the NRR process, the ^{1}H NMR spectrum exhibited the doublets for $^{15}NH_4^+$ at $^{15}J_{N\text{-}H} = 72$ Hz (Fig. 4 g). In contrast, when the $^{14}N_2$ source was used, $^{14}NH_4^+$ was formed as evident from its characteristic triplet peaks with $^{14}J_{N\text{-}H} = 52$ Hz [33]. These results confirm that the 5% In-Bi_2MoO_6 efficiently accomplishes "overall nitrogen fixation", converting N_2 into ammonia and subsequently oxidizing it into nitrate under mild conditions.

The photocatalytic stability of 5% In-Bi_2MoO_6 samples for overall nitrogen fixation is shown in Fig. 4 h and S7. As seen, the photocatalyst maintained its activity through 5 continuous cycles, and post-cycling XRD (Fig. S8), SEM, TEM (Fig. S9), and XPS (Fig. S10) examination demonstrates that no substantial compositional changes have occurred, confirming its good stability. Furthermore, the AQY of photocatalytic NH_3 reached 1.4% at 365 nm, indicating its high incident light usage efficiency (Fig. 4i).

3.3. Photocatalytic "overall nitrogen fixation" mechanism

The charge separation and transfer efficiency of photogenerated carriers in 5% In-Bi_2MoO_6 was evaluated using transient photocurrent measurement, EIS, and PL spectra [34]. Fig. 5a reveals that 5% In-Bi_2MoO_6 has a higher transient photocurrent than Bi_2MoO_6, suggesting the photocatalyst's strong photogenerated charge carrier ability [34]. Fig. 5b shows the EIS-based Nyquist plots where the smaller semi-circle radius of 5% In-Bi_2MoO_6 confirmed its superior charge carrier transportation compared to the In-free counterpart. The ohmic resistance (R_1) and charge transfer resistance (R_2) between photocatalyst and electrolyte are shown as an inset Fig. 5b. The R_1 of Bi_2MoO_6 and 5% In-Bi_2MoO_6 is comparable, the charge transfer resistance (6445 Ω) of 5% In-Bi_2MoO_6 is substantially lower than that of Bi_2MoO_6 (10912 Ω), confirming former's efficient carrier transfer ability at the photocatalyst/solution interface [35]. The decreased PL intensity of 5% In-Bi_2MoO_6 further confirmed its lower electron-hole recombination rate (Fig. 5c) [36]. The average lifetime (τ_{av}) of photogenerated carriers deduced from time-resolved photoluminescence (TR-PL) indicates improved average life of 0.307 ns for 5% In-Bi_2MoO_6 compared to Bi_2MoO_6 (1.684 ns) (Fig. 5d). This slower decay rate indicates that In^{3+} doping effectively inhibits the recombination of photo-generated e^-/h^+ pairs and prolongs the carrier lifetime [37]. The Mott-Schottky plots are shown in Figs. 5e and S11, 5% In-Bi_2MoO_6 shows a relatively smaller slope than Bi_2MoO_6, indicating a faster charge transfer and a higher donor density. The carrier densities (N_d) of the samples can be calculated from the slopes of Mott-Schottky plots according to Eq. 5 [38].

$$N_d = 2\Big/(e_0\varepsilon\varepsilon_0)[d/(1/C^2)/dV]^{-1} \tag{5}$$

where e_0 is the electron charge (1.6×10^{-19} C), ε is the dielectric constant of Bi_2MoO_6. ε_0 is the vacuum dielectric constant (8.86×10^{-12} F m^{-1}), and V is the applied bias at the electrode. 5% In-Bi_2MoO_6 (6.59×10^{20} cm^{-3}) can be seen to exhibit the higher carrier density than pristine Bi_2MoO_6 (4.59×10^{20} cm^{-3}) at the frequency of 600 Hz.

The Mott-Schottky plots were deduced to evaluate bandgap alteration in 5% In-Bi_2MoO_6. Flat band potentials (E_{fb}) of 5% In-Bi_2MoO_6 and Bi_2MoO_6 were calculated to be -0.76 and -0.5 V vs. Ag/AgCl, respectively (or -0.56 and -0.3 V vs. NHE). Furthermore, the positive line slopes indicate that doped Bi_2MoO_6 is an n-type semiconductor [39]. The conduction band of an n-type semiconductor is typically 0.1–0.3 V more negative than E_{fb} [40]. The predicted E_{CBM} values of 5% In-Bi_2MoO_6 and Bi_2MoO_6 were -0.66 and -0.4 V vs. NHE, respectively, which were more negative than the conventional redox potential of N_2/NH_3 (-0.28 V vs. NHE). The maximum valence band position was deduced from X-ray photoelectron spectra (VB-XPS). The valence band edge potentials of 5% In-Bi_2MoO_6 and Bi_2MoO_6 were predicted to be 1.99 and 2.18 V, respectively, as shown in Fig. 5f and S12. According to the empirical formula: $E_{VBM} = E_{CBM} + E_g$, the minimum conduction band (CBM) of Bi_2MoO_6 and 5% In-Bi_2MoO_6 are -0.4 and -0.52 V, respectively.

The photoelectron migration behavior of photogenerated electron/hole pairs is further investigated by the ESR under illumination. Fig. 6 shows the signals for superoxide radical ($\cdot O_2^-$) and hydroxyl radical (•OH) that aided in predicting the ammonia production process indirectly based on the oxidation or reduction half-reaction occurring at the VB (or CB) of the photocatalyst. Typical two signal peaks with peak height ratios of 1:2:2:1 (DMPO-·OH) and 1:1:1:1 (DMPO-·O_2^-) were identified. Furthermore, the 5% In-Bi_2MoO_6 was assessed for O_2

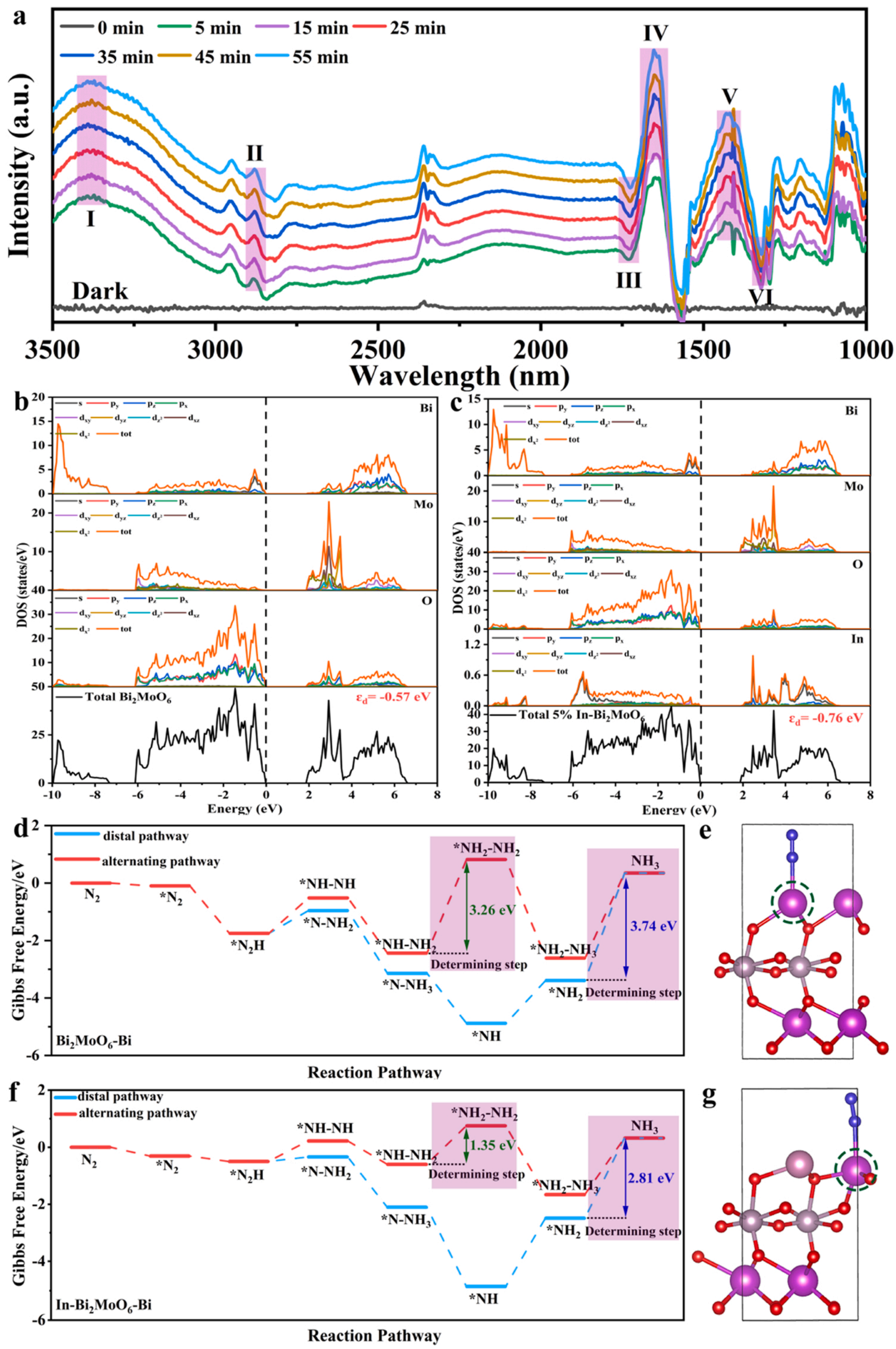

Fig. 8. (a) In situ FTIR spectra of 5% In-Bi_2MoO_6 in the dark and under light irradiation for up to 55 min. The calculated DOS of (b) Bi_2MoO_6, (c) 5% In-Bi_2MoO_6. Gibbs free energy diagrams of NRR for (d) Bi_2MoO_6, (f) In-Bi_2MoO_6-Bi. (e, g) Models of possible active sites for Bi_2MoO_6-Bi (001) surface, In-Bi_2MoO_6-Bi.

production in (a) N_2, (b) Air, and (c) Ar atmospheres using DMPO as a scavenger (Fig. 6a-c). As seen in the usual ESR signal of 5% In-Bi_2MoO_6, the intensity of $\cdot O_2^-$ production drops, indicating the photocatalyst's exceptional ability to oxidize water in a N_2 environment. Additionally, the •OH generated by 5% In-Bi_2MoO_6 also followed a similar trend (Fig. 6d-f). 5% In-Bi_2MoO_6 can overcome thermodynamic barriers and efficiently generate hydroxyl (·OH) and superoxide radicals ($\cdot O_2^-$) due to its more negative potential than superoxide radical (E ($O_2/\cdot O_2^-$) = −0.33 V vs NHE) and its more positive potential than hydroxyl radical (E (·OH/OH^-) = 1.99 V vs NHE).

Since, VBM potentials of Bi_2MoO_6 (2.18 V) and 5% In-Bi_2MoO_6 (1.99 V) were determined to be greater than E^0 (NH_3/NO_3^- = +0.36 V vs NHE), photocatalyst could effectively generate NH_3, which may be further oxidize to NO_3^- (NH_3 + ·OH → NO_3^-) [41]. Fig. 7 depicts a bandgap-based illustration demonstrating improved photocatalytic "overall nitrogen fixation" reaction of 5% In-Bi_2MoO_6.

In-situ infrared experiment was used to further study the adsorption and activation of 5% In-Bi_2MoO_6 on the surface and the reaction mechanism of nitrogen fixation (Fig. 8a). After dark adsorption equilibrium, in which a series of vibrational bands can be clearly identified.

Among them, peak I (3385 cm^{-1}) was corresponded to the stretching vibration of N-H, peak II (2882 cm^{-1}) and peak VI (1431 cm^{-1}) were ascribed to NH_4^+ characteristic absorption peaks [42], peak III 1723 cm^{-1} was assigned to NH_3 characteristic absorption peak [43]. Peak IV (1649 cm^{-1}) was attributed to the $*N_2$ molecular characteristic absorption peaks [44]. The peak V (1380 cm^{-1}) was ascribed to NO_3^-. Furthermore, the peaks I, II, VI, and V are significantly enhanced in intensity with the prolongation of light irradiation, while peaks III and IV have the intensity of the increase diminished, indicating the transformation process of $N_2 \rightarrow NH_3/NH_4^+ \rightarrow NO_3^-$ via a relay catalysis on In-Bi_2MoO_6.

DFT calculations were carried out to further elucidate the fundamental mechanism for electronic structure modulation in Bi_2MoO_6 via In^{3+} doping. The total and partial density states of Bi_2MoO_6 and In-doped Bi_2MoO_6 are shown in Fig. 8b-c, respectively, with a dashed vertical line designating the Fermi level (E_F). O 2p orbitals made up most of the VB for Bi_2MoO_6, while Bi 6p, O 2p, and Mo 3d orbitals made up the majority of the CB [45]. Owing to introduction of In, the orbitals of internally doped Bi_2MoO_6 are mainly contributed by Bi 6p, Mo 3d and In 3d. The band gap of In-doped Bi_2MoO_6 (2.51 eV) was smaller than those in undoped Bi_2MoO_6 (2.58 eV) with the corresponding D-band center of − 0.76 and − 0.57 eV [46], respectively. It is known that the adsorption and activation of N_2 on the H_2O/catalyst interface are critical to the N_2 fixation reaction. The electrons can transfer from the bonding orbital ($2\sigma_g$) of the N_2 molecule to the transition metal D-orbital to form an adsorption state ($*N_2$). During photocatalytic N_2 fixation, the electron in the D-orbital can donated from metal (Bi or In site) to the antibonding orbital (π^*) of N_2 to form the activated state ($*N_2$) at the H_2O/In-Bi_2MoO_6 interface. Simultaneously, H_2O is oxidized by the photogenerated hole in VB and releases protons. The $*N_2$ accepts electrons from CB and combines with protons, undergoing a multi-electron hydrogenation process to be converted into NH_3/NH_4^+ [47,48]. Given that In-doping precisely optimized the electronic structure of Bi_2MoO_6, the D-band center shifted up, which might be benefit for N_2 molecule physical/chemical adsorption, activation and hydrogenation.

The influence of In^{3+} doping on Gibbs free energy during the NRR process of the distal associative and alternative associative mechanism is shown in Fig. 8d-g. The distal associative mechanism, the nitrogen atom farthest from the catalysts is combine with the H^+ and electron of CB, followed by the second H^+ until the ammonia molecule is produced. The alternative associative mechanism is the hydrogenation of the two nitrogen atoms, which occurs simultaneously in the alternate associative route [49,50]. Obviously, In-Bi_2MoO_6 showed better N_2 activation performance ($* + N_2 \rightarrow *N_2$) than Bi_2MoO_6, which is beneficial to subsequent hydrogenation reaction. Generally, the first hydrogenation step ($*N_2 + H^+ + e^- \rightarrow *N\text{-}NH$) in each of these routes is identical, but the subsequent hydrogenation stages change due to distinct processes. For Bi_2MoO_6 Bi active sites, the rate-determining steps exhibit the high ΔG values based on the two mechanisms (3.74 and 3.26 eV, respectively); thus, Bi_2MoO_6 Bi sites may not favor NRR (Fig. 8d-e). Interestingly, for the In-Bi_2MoO_6 Bi site, ΔG values of the rate-determining steps based on the mechanisms mentioned above are 2.81 and 1.35 eV, respectively (Fig. 8f-g). Furthermore, the ΔG value based on two mechanisms for In-Bi_2MoO_6 In site is 2.78 and 2.24 eV, respectively (Fig. S13a-b). It is clear that In^{3+} doping greatly reduces the activation energy of the rate-determining steps at different active sites based on distal associative and alternative associative mechanisms, which indicates a high possibility of activation of N_2 and spontaneous hydrogenation on In-Bi_2MoO_6 at the Bi site and In site under solar irradiation. It prefers to proceed via the alternating pathway for the In-doped Bi_2MoO_6 In site, based on its thermodynamic favourability for the NRR reaction. Accordingly, the DFT calculations further testified that indium doping has significantly altered the D-band center, achieving a lower energy barrier that could be anticipated for nitrogen chemisorption/activation and the subsequent hydrogenation reaction at H_2O/In-Bi_2MoO_6 interface.

4. Conclusion

In conclusion, an In-doped Bi_2MoO_6 photocatalyst was prepared using a simple solvothermal method to achieve an overall nitrogen fixating reaction. To achieve optimum performance, In content was varied in the range of 1–10%, where 5% In-Bi_2MoO_6 realized the best photocatalytic performance reaching the highest NH_3 and NO_3^- production rate of 53.4 and 54 $\mu mol \cdot g^{-1} \cdot h^{-1}$, respectively. The optimum In doping (5% In-Bi_2MoO_6) realized 1.4 folds higher charge-carrier density under illumination with expedited spatial separation/transfer and extended charge-carrier lifespan compared to pristine Bi_2MoO_6. Moreover, thermodynamic assessment of the catalyst further elucidated the reaction mechanism, which follows a low Gibbs energy pathway involving hydrogenation of $*N_2$ over the catalytic surface to NH_3/NH_4^+, which subsequently oxidizes to NO_3^-, accomplishing "overall nitrogen fixation". The DFT based calculations supported the partial substitution of Bi^{3+} with In^{3+} in the main crystal of Bi_2MoO_6, altering its electronic structure and resulting in a lower energy barrier for nitrogen chemisorption/activation and the subsequent hydrogenation reaction. The suggested transition metal-doped modification approach for customizing photocatalysts proved highly efficient for clean, energy-efficient, and cost-effective ammonia and nitrate production. In a word, the present work provides a new vista of green "overall nitrogen fixation" via a novel relay catalysis.

CRediT authorship contribution statement

Taoxia Ma: Methodology, Data curation, Writing. **Chunming Yang**: Conceptualization, Supervision, Writing – review & editing. **Li Guo**: Investigation, Methodology, Validation. **Razium Ali Soomro**: Writing – review & editing. **Danjun Wang**: Conceptualization, Writing – review & editing, Funding acquisition. **Bin Xu**: Resources, Validation. **Feng Fu**: Validation, Resources, Supervision.

Declaration of Competing Interest

The authors declare that they have no known competing financial interests or personal relationships that could have appeared to influence the work reported in this paper.

Data Availability

Data will be made available on request.

Acknowledgments

This work was financially supported by the National Natural Science Foundation of China (No. 22168040, 22162025) and the Project of Science & Technology Office of Shaanxi Province (No. 2022JM-062).

Appendix A. Supporting information

Supplementary data associated with this article can be found in the online version at doi:10.1016/j.apcatb.2023.122643.

References

[1] G.F. Chen, Y. Yuan, H. Jiang, S.Y. Ren, L.X. Ding, L. Ma, T. Wu, J. Lu, H. Wang, Electrochemical reduction of nitrate to ammonia via direct eight-electron transfer using a copper–molecular solid catalyst, Nat. Energy 5 (2020) 605–613.
[2] A. Biswas, S. Kapse, R. Thapa, R.S. Dey, Oxygen functionalization-induced charging effect on boron active sites for high-yield electrocatalytic NH_3 production, Nano-Micro Lett. 14 (2022) 1–17.
[3] Y. Fu, Y. Liao, P. Li, H. Li, S. Jiang, H. Huang, W. Sun, T. Li, H. Yu, K. Li, Layer structured materials for ambient nitrogen fixation, Coord. Chem. Rev. 460 (2022), 214468.

[4] N. Zhang, A. Jalil, D. Wu, S. Chen, Y. Liu, C. Gao, W. Ye, Z. Qi, H. Ju, C. Wang, Refining defect states in $W_{18}O_{49}$ by Mo doping: a strategy for tuning N_2 activation towards solar-driven nitrogen fixation, J. Am. Chem. Soc. 140 (2018) 9434–9443.
[5] X. Zhang, R. Shi, Z. Li, J. Zhao, H. Huang, C. Zhou, T. Zhang, Photothermal-assisted photocatalytic nitrogen oxidation to nitric acid on palladium-decorated titanium oxide, Adv. Energy Mater. 12 (2022), 2103740.
[6] M. Kuang, Y. Wang, W. Fang, H. Tan, M. Chen, J. Yao, C. Liu, J. Xu, K. Zhou, Q. Yan, Efficient nitrate synthesis via ambient nitrogen oxidation with Ru-doped TiO_2/RuO_2 electrocatalysts, Adv. Mater. 32 (2020), 2002189.
[7] S. Licht, B. Cui, B. Wang, F.F. Li, J. Lau, S. Liu, Ammonia synthesis by N_2 and steam electrolysis in molten hydroxide suspensions of nanoscale Fe_2O_3, Science 345 (2014) 637–640.
[8] M.A. Légaré, G. Bélanger Chabot, R.D. Dewhurst, E. Welz, I. Krummenacher, B. Engels, H. Braunschweig, Nitrogen fixation and reduction at boron, Science 359 (2018) 896–900.
[9] Y. Sun, Z. Deng, X.M. Song, H. Li, Z. Huang, Q. Zhao, D. Feng, W. Zhang, Z. Liu, T. Ma, Bismuth-based free-standing electrodes for ambient-condition ammonia production in neutral media, Nano-Micro Lett. 12 (2020) 1–12.
[10] P. Xia, X. Pan, S. Jiang, J. Yu, B. He, P.M. Ismail, W. Bai, J. Yang, L. Yang, H. Zhang, Designing a redox heterojunction for photocatalytic "overall nitrogen fixation" under mild conditions, Adv. Mater. 34 (2022), 2200563.
[11] X. Jin, L. Ye, H. Xie, G. Chen, Bismuth-rich bismuth oxyhalides for environmental and energy photocatalysis, Coord. Chem. Rev. 349 (2017) 84–101.
[12] S.S. Bhat, H.W. Jang, Recent advances in bismuth-based nanomaterials for photoelectrochemical water splitting, ChemSusChem 10 (2017) 3001–3018.
[13] P. Li, S. Gao, Q. Liu, P. Ding, Y. Wu, C. Wang, S. Yu, W. Liu, Q. Wang, S. Chen, Recent progress of the design and engineering of bismuth oxyhalides for photocatalytic nitrogen fixation, Adv. Energy Sustain. Res 2 (2021), 2000097.
[14] Y. Wang, M.M. Shi, D. Bao, F.L. Meng, Q. Zhang, Y.T. Zhou, K.H. Liu, Y. Zhang, J. Z. Wang, Z.W. Chen, Generating Defect-rich bismuth for enhancing the rate of nitrogen electroreduction to ammonia, Angew. Chem. Int. Ed. 131 (2019) 9564–9569.
[15] L. Li, C. Tang, B. Xia, H. Jin, Y. Zheng, S.Z. Qiao, Two-dimensional mosaic bismuth nanosheets for highly selective ambient electrocatalytic nitrogen reduction, ACS Catal. 9 (2019) 2902–2908.
[16] Y. Hao, X. Dong, S. Zhai, H. Ma, X. Wang, X. Zhang, Hydrogenated bismuth molybdate nanoframe for efficient sunlight-driven nitrogen fixation from air, Chem. Eur. J. 22 (2016) 18722–18728.
[17] Y. Sun, Y. Ahmadi, K.H. Kim, J. Lee, The use of bismuth-based photocatalysts for the production of ammonia through photocatalytic nitrogen fixation, Renew. Sust. Energ. Rev. 170 (2022), 112967.
[18] Y. Bo, H. Wang, Y. Lin, T. Yang, R. Ye, Y. Li, C. Hu, P. Du, Y. Hu, Z. Liu, Altering hydrogenation pathways in photocatalytic nitrogen fixation by tuninag local electronic structure of oxygen vacancy with dopant, Angew. Chem. Int. Ed. 60 (2021) 16085–16092.
[19] P. Qiu, C. Huang, G. Dong, F. Chen, F. Zhao, Y. Yu, X. Liu, Z. Li, Y. Wang, Plasmonic gold nanocrystals simulated efficient photocatalytic nitrogen fixation over Mo doped $W_{18}O_{49}$ nanowires, J. Mater. Chem. A. 9 (2021) 14459–14465.
[20] P. Chang, Y. Wang, Y. Zhu, Current trends on In_2O_3 based heterojunction photocatalytic systems in photocatalytic application, Chem. Eng. J. 450 (2022), 137804.
[21] S. Wang, F. Ichihara, H. Pang, H. Chen, J. Ye, Nitrogen fixation reaction derived from nanostructured catalytic materials, Adv. Funct. Mater. 28 (2018), 1803309.
[22] J. Tian, P. Hao, N. Wei, H. Cui, H. Liu, 3D Bi_2MoO_6 nanosheet/TiO_2 nanobelt heterostructure: enhanced photocatalytic activities and photoelectochemistry performance, ACS Catal. 5 (2015) 4530–4536.
[23] Y. Zhang, L. Guo, Y. Wang, T. Wang, T. Ma, Z. Zhang, D. Wang, B. Xu, F. Fu, In-situ anion exchange based Bi_2S_3/OV-Bi_2MoO_6 heterostructure for efficient ammonia production: A synchronized approach to strengthen NRR and OER reactions, J. Mater. Sci. Technol. 110 (2022) 152–160.
[24] J. Zhang, G. Zhu, S. Li, F. Rao, Q.U. Hassan, J. Gao, Y. Huang, M. Hojamberdiev, Novel Au/La-Bi_5O_7I microspheres with efficient visible-light photocatalytic activity for NO removal: synergistic effect of Au nanoparticles, La doping, and oxygen vacancy, ACS Appl. Mater. Interfaces 11 (2019) 37822–37832.
[25] X. Chen, M.Y. Qi, Y.H. Li, Z.R. Tang, Y.J. Xu, Enhanced ambient ammonia photosynthesis by Mo-doped Bi_5O_7Br nanosheets with light-switchable oxygen vacancies, Chin. J. Catal. 42 (2021) 2020–2026.
[26] G. Zhang, D. Chen, N. Li, Q. Xu, H. Li, J. He, J. Lu, Fabrication of Bi_2MoO_6/ZnO hierarchical heterostructures with enhanced visible-light photocatalytic activity, Appl. Catal. B: Environ. 250 (2019) 313–324.
[27] P. Zhang, D. Wang, Q. Zhu, N. Sun, F. Fu, B. Xu, Plate-to-layer Bi_2MoO_6/MXene-heterostructured anode for lithium-ion batteries, Nano-Micro Lett. 11 (2019) 1–14.
[28] Y. Liu, C. Chen, Y. He, Z. Zhang, M. Li, C. Li, X.B. Chen, Y. Han, Z. Shi, Rich indium-vacancies In_2S_3 with atomic p–n homojunction for boosting photocatalytic multifunctional properties, Small 18 (2022), 2201556.
[29] X. Wang, Z. Wang, Y. Li, J. Wang, G. Zhang, Efficient photocatalytic CO_2 conversion over 2D/2D Ni-doped $CsPbBr_3/Bi_3O_4Br$ Z-scheme heterojunction: Critical role of Ni doping, boosted charge separation and mechanism study, Appl. Catal. B: Environ. 319 (2022), 121895.
[30] J. Yang, Y. Guo, R. Jiang, F. Qin, H. Zhang, W. Lu, J. Wang, J.C. Yu, High-efficiency "working-in-tandem" nitrogen photofixation achieved by assembling plasmonic gold nanocrystals on ultrathin titania nanosheets, J. Am. Chem. Soc. 140 (2018) 8497–8508.
[31] Q. Liu, H. Tian, Z. Dai, H. Sun, J. Liu, Z. Ao, S. Wang, C. Han, S. Liu, Nitrogen-doped carbon nanospheres-modified graphitic carbon nitride with outstanding photocatalytic activity, Nano-Micro Lett. 12 (2020) 1–15.
[32] J. Zander, J. Timm, M. Weiss, R. Marschall, Light-induced ammonia generation over defective carbon nitride modified with pyrite, Adv. Energy Mater. 12 (2022), 2202403.
[33] J. Di, C. Chen, Y. Wu, Y. Zhao, C. Zhu, Y. Zhang, C. Wang, H. Chen, J. Xiong, M. Xu, Polarized Cu–Bi site Pairs for non-covalent to covalent interaction tuning toward N_2 photoreduction, Adv. Mater. 34 (2022), 2204959.
[34] Y. Yang, Y.X. Pan, X. Tu, C.J. Liu, Nitrogen doping of indium oxide for enhanced photocatalytic reduction of CO_2 to methanol, Nano Energy 101 (2022), 107613.
[35] Q. You, C. Zhang, M. Cao, B. Wang, J. Huang, Y. Wang, S. Deng, G. Yu, Defects controlling, elements doping, and crystallinity improving triple-strategy modified carbon nitride for efficient photocatalytic diclofenac degradation and H_2O_2 production, Appl. Catal. B: Environ. 321 (2022), 121941.
[36] G. Ba, T. Huo, Q. Deng, H. Li, W. Hou, Mechanochemical synthesis of nitrogen-deficient mesopore-rich polymeric carbon nitride with highly enhanced photocatalytic performance, ACS Sustain. Chem. Eng. 8 (2020) 18606–18615.
[37] W. Zhao, Y. Feng, H. Huang, P. Zhou, J. Li, L. Zhang, B. Dai, J. Xu, F. Zhu, N. Sheng, A novel Z-scheme $Ag_3VO_4/BiVO_4$ heterojunction photocatalyst: study on the excellent photocatalytic performance and photocatalytic mechanism, Appl. Catal. B: Environ. 245 (2019) 448–458.
[38] S. Gao, H. Ji, P. Yang, M. Guo, J. Tressel, S. Chen, Q. Wang, High-performance photocatalytic reduction of nitrogen to ammonia driven by oxygen vacancy and ferroelectric polarization field of $SrBi_4Ti_4O_{15}$ nanosheets, Small 19 (2023), 2206114.
[39] Y. Wu, P. Xiong, J. Wu, Z. Huang, J. Sun, Q. Liu, X. Cheng, J. Yang, J. Zhu, Y. Zhou, Band engineering and morphology control of oxygen-incorporated graphitic carbon nitride porous nanosheets for highly efficient photocatalytic hydrogen evolution, Nano-Micro Lett. 13 (2021) 1–12.
[40] T. Wang, J. Liu, P. Wu, C. Feng, D. Wang, H. Hu, G. Xue, Direct utilization of air and water as feedstocks in the photo-driven nitrogen reduction reaction over a ternary Z-scheme SiW_9Co_3/PDA/BWO hetero-junction, J. Mater. Chem. A. 8 (2020) 16590–16598.
[41] L. Ye, C. Han, Z. Ma, Y. Leng, J. Li, X. Ji, D. Bi, H. Xie, Z. Huang, Ni_2P loading on $Cd_{0.5}Zn_{0.5}S$ solid solution for exceptional photocatalytic nitrogen fixation under visible light, Chem. Eng. J. 307 (2017) 311–318.
[42] P. Li, Z. Zhou, Q. Wang, M. Guo, S. Chen, J. Low, R. Long, W. Liu, P. Ding, Y. Wu, Visible-light-driven nitrogen fixation catalyzed by Bi_5O_7Br nanostructures: enhanced performance by oxygen vacancies, J. Am. Chem. Soc. 142 (2020) 12430–12439.
[43] S. Gao, R. Wu, M. Sun, M. Guo, D.B. DuBois, S. Chen, H. Ji, C. Wang, Q. Wang, High-performance nitrogen photofixation by $Bi_2Sn_2O_7$ nanoparticles enriched with oxygen vacancies, Appl. Catal. B: Environ. 324 (2023), 122260.
[44] X. Liu, Y. Luo, C. Ling, Y. Shi, G. Zhan, H. Li, H. Gu, K. Wei, F. Guo, Z. Ai, Rare earth La single atoms supported MoO_{3-x} for efficient photocatalytic nitrogen fixation, Appl. Catal. B: Environ. 301 (2022), 120766.
[45] J. Guo, L. Shi, J. Zhao, Y. Wang, K. Tang, W. Zhang, C. Xie, X. Yuan, Enhanced visible-light photocatalytic activity of Bi_2MoO_6 nanoplates with heterogeneous Bi_2MoO_{6-x}@Bi_2MoO_6 core-shell structure, Appl. Catal. B: Environ. 224 (2018) 692–704.
[46] D.K. Yesudoss, H. Chun, B. Han, S. Shanmugam, Accelerated N_2 reduction kinetics in hybrid interfaces of $NbTiO_4$ and nitrogen-doped carbon nanorod via synergistic electronic coupling effect, Appl. Catal. B: Environ. 304 (2022), 120938.
[47] T. Wang, C. Feng, J. Liu, D. Wang, H. Hu, J. Hu, Z. Chen, G. Xue, Bi_2WO_6 hollow microspheres with high specific surface area and oxygen vacancies for efficient photocatalysis N_2 fixation, Chem. Eng. J. 414 (2021), 128827.
[48] W. Guo, K. Zhang, Z. Liang, R. Zou, Q. Xu, Electrochemical nitrogen fixation and utilization: theories, advanced catalyst materials and system design, Chem. Soc. Rev. 48 (2019) 5658–5716.
[49] Y. Wei, W. Jiang, Y. Liu, X. Bai, D. Hao, B.J. Ni, Recent advances in photocatalytic nitrogen fixation and beyond, Nanoscale 14 (2022) 2990–2997.
[50] J. Zhao, Z. Chen, Single Mo atom supported on defective boron nitride monolayer as an efficient electrocatalyst for nitrogen fixation: a computational study, J. Am. Chem. Soc. 139 (2017) 12480–12487.